Gas-Phase Ion Chromatography: Transition Metal State Selection and Carbon Cluster Formation

Michael T. Bowers,* Paul R. Kemper, Gert von Helden, Petra A. M. van Koppen

Gas-phase ion chromatography can separate ions that have the same mass but differ in isomeric structure or electronic configuration. The main features of this technique are briefly outlined, and applications to a series of problems in transition metal chemistry and carbon cluster chemistry are described. Examples in transition metal chemistry include state-selective reactivity, excited state deactivation, and state-selective ligand binding energies. For clusters, ion chromatography was used to determine the structure of pure carbon cluster ions as a function of size from C_4 to C_{84}. The results indicate that carbon grows first in linear chains, transforms to monocyclic planar rings at about C_{10}, and forms new families of planar bi-, tri-, and tetracyclic rings at C_{20}, C_{30}, and C_{40}, respectively. Fullerenes, which mysteriously appear at C_{30} and dominate by C_{50}, are generated by heating the planar ring systems above an isomerization barrier rather than by growth of graphite precursors.

During the last several decades, gas-phase ion chemistry has played a crucial role in the understanding of the fundamental aspects of the kinetics, energetics, and dynamics of chemical reactions. Modern analytical chemistry relies heavily on the use of mass spectrometry and ion molecule reactions for the characterization of chemical systems. However, a fundamental problem in most modern techniques used in the study of gas-phase ions is their insensitivity to the structure and electronic state of the ion. Recently we developed the technique of ion chromatography (IC), which allows us to address many of these problems. In this article, we describe the development and some important applications of this technique.

The study of ions drifting in gases started in earnest at the beginning of this century, although James Clerk Maxwell (*1*) first published a momentum transfer theory of diffusion in 1860. The first quantitative "low-field" theory of ion mobility was published by Langevin (*2*) in 1905, and many of the key elements of this theory hold today. Effects caused by stronger electric fields were most effectively developed by Wannier (*3*) in 1953, and these ideas and equations are still in use. Full discussions of the historical development of ion mobility are given (*4–6*). Of importance here is the basic definition of ion mobility

$$v_d = KE \qquad (1)$$

where K is the mobility, v_d is the ion drift velocity, and E is the electric field to which the ion is subject. With the use of IC, mobilities are simply and accurately measured and are then theoretically related to important molecular parameters. For example, IC can separate electronic configurations of transition metal ions, allowing the study of the state-selected chemistry of these species at thermal energies. Also, IC is used to separate and unambiguously identify the structures of carbon cluster ions as a function of cluster size. These very different but equally important applications show the versatility of the method and suggest important new problems to tackle, particularly on macromolecular ions.

The use of ion mobility has not been overlooked by others. In fact, an analytical device operating at atmospheric pressure has been developed [the ion mobility spectrometer (IMS)] and applied to a number of important environmental and other problems (*7–9*). The field in which the IMS is used remains active and lively and appears to have a bright future in such areas as forensic science (*10*). Most applications of this method will remain in applied analytical science, however, because of the intrinsic limitations brought on by operation at atmospheric pressure: none of the applications of IC described in this article can utilize the IMS. In any case, the IMS method plays an important analytical role and is directed toward goals other than those discussed here.

Experimental

A detailed description of the apparatus (*11*) will not be repeated here, but a functional description will be given. A number of ion sources are available for the experiments described. These include a traditional electron ionization (EI) source, a surface ionization (SI) source, and a laser desorption and supersonic expansion (LD-SSE) source. The EI and SI sources are used for the transition metal ion chemistry and the LD-SSE source for carbon clusters. The EI source is standard and forms ions by high-energy electron impact. The SI source is similar to one developed by Armentrout (*12*) and forms ions by thermal heating on a very hot filament (2250 ± 200 K). Our version allows standard EI as well as SI to be used with the same sample (*13*). Having both sources simultaneously available is very useful.

The LD-SSE source is a variant of the Smalley laser desorption source (*14*) that can float at 5 kV for use with sector mass spectrometers (*15*). Intense cluster beams, both positively and negatively charged, are formed without external ionization. Further, the distance from the laser desorption point to the SSE nozzle can be very short, allowing nearly "nascent" or "early growth" cluster distributions to be obtained. This feature is critical for our carbon cluster studies.

The chromatography cell (Fig. 1) is the key part of the experiment. In a typical experiment, mass-selected ions are injected through a small hole at low energies (1 to 5 eV in the lab frame of reference, <0.1 eV center of mass) into the cell filled with 2 to 5 torr of He with a small amount of reactant gas, if needed ($\sim 10^{-5}$ to 10^{-3} torr). The ions are rapidly thermalized as they enter the cell. The ions drift through the cell under the influence of a weak electronic field (typically 1 to 10 V cm^{-1}) in t_d = 100 to 1000 μs and experience 10^4 to 10^5 collisions with He. The time it takes an ion to traverse the cell depends on its mobility, which in turn depends inversely on the collision cross section of the species with He gas: the larger the cross section, the smaller the mobility and the longer the time. Realizing that the drift velocity $v_d = z/t_d$, where z is the cell length, and the mobility $K \cong A/\sigma$, where σ is the collision cross section (*16*) and A is a constant term that incorporates known properties of the system (mass, charge, and temperature) (*17*), we have from Eq. 1 for ions of fixed mass

$$t_d = \frac{z\sigma}{AE} \qquad (2)$$

From Eq. 2 a very important property

Department of Chemistry, University of California, Santa Barbara, CA 93106.

*To whom correspondence should be addressed.

emerges; namely, the time the ion spends in the chromatography cell is directly proportional to the collision cross section of that ion with the bath gas. Thus, for two different species of the same mass

$$t_d(1) = \frac{\sigma(1)}{\sigma(2)}\, t_d(2) \qquad (3a)$$

$$t_d(1) - t_d(2) = \frac{z}{AE}\,[\sigma(1) - \sigma(2)] \qquad (3b)$$

where the numbers in parentheses refer to ion type. Hence, if a very short pulse of ions is injected into the cell, ions of different types will exit at different times, even if they have the same mass. These effects can be very large, and an unprecedented type of information can be obtained.

One factor that affects the utility of the device is resolution. It is straightforward to show (*18*) that the resolution is given by

$$\frac{t_d}{\Delta t_d} = \left(\frac{qV}{8kT}\right)^{1/2} \qquad (4)$$

where Δt_d is the time width of an ion packet of a specific species attributable to collisional broadening in the cell, q is the ion charge, V is the voltage drop across the cell, k is the Boltzmann constant, and T is the temperature. In the ideal case, $\Delta t_d << [t_d(1) - t_d(2)]$ so that abundances of ions having different collision cross sections can be clearly resolved. As is apparent from Eq. 4, the resolution increases (Δt_d decreases) in proportion to $(V/T)^{1/2}$. Hence, for resolution purposes, higher values of V and lower values of T are desirable.

We have, in fact, shown (*18*) dramatic increases in resolution for transition metal ions by reducing T from 300 to 150 K. As temperature becomes very low, however, the improved resolution cannot overcome the fact that $\sigma(1) \cong \sigma(2)$ as $T \rightarrow 0$. Because operation at these extremely low temperatures is not practical experimentally, this limitation is not serious.

Unfortunately, an increase in V requires a simultaneous increase in bath gas pressure to avoid "translational heating" of the ions and loss of resolution. Our instrument has an effective upper limit of ~5 torr (attributable to pumping speed restrictions); however, we do observe a significant improvement in signal in going from 2 to 5 torr, as expected. In reality, an increase in resolution by an increase in pressure reduces signal intensity; our experiments reflect a balance of the intensity and resolution effects.

Finally, once the ions leave the chromatography cell, they are mildly accelerated and passed through a quadrupole mass filter. Thus, ions that arrive at the detector can be unambiguously identified, a necessary feature for reactivity or collision-induced dissociation and annealing studies. Single-ion counting methods maximize signal detection efficiency. We focus on two major applications of IC: state-selected chemistry of transition metal ions and the isomer structure, abundance, and growth mechanisms in carbon cluster ions.

Transition Metal Ions

We first discovered (*11*) the ability of He gas to "chromatographically" or "electrophoretically" separate electronic configurations of transition metal ions while attempting to determine the amount of time Co^+ ions spent in the cell so that we could derive reaction rate constants. To our surprise, pulsing experiments generated bimodal arrival time distributions (ATDs) for Co^+ that were baseline resolved (Fig. 2). After many diagnostic experiments, we convinced ourselves that the signal was real (*19*) and then quickly proceeded to show that essentially all first row transition metal ions demonstrate the same bimodal behavior (*18*). Because the energies and electron configurations of the ground states and low-lying metastable (long-lived) excited states of first row transition metals were all well known and because we could unambiguously show which of the two peaks corresponded to the ground state (by lowering the ionizing energy to near threshold values), we determined that $3d^n$ configurations had low mobilities (longer time peak) and that $3d^{n-1}4s$ configurations had mobilities that were ~50% larger (shorter time peak). In fact, the $3d^n$ mobilities were precisely predicted by simple Langevin capture theory, indicating that the small $3d^n$ transition metal ions were undergoing capture collisions with He. We then rationalized that the "faster than Langevin" peaks were a result of repulsive interactions of the 4*s* orbital on the metal with the filled $1s^2$ orbital of He, which prevented capture collisions from occurring. As a consequence, the M^+ ($3d^{n-1}4s^1$) ions proceeded rapidly through the He bath gas.

The electronic state population of transition metal ions can be changed in a completely known way simply by varying formation conditions (such as ionizing electron energy, compound used, and surface ionization), and often these changes span a broad range (in the case of Co^+, from 97 to 36% ground state) (Fig. 2). Consequently, we could address the question of electronic state–specific reactivity of transition metal ions with neutral molecules, an area of intense interest, but one fraught with difficulty when traditional experimental methods are used (*20, 21*).

State-selected reactivity. In the past 2 years, we have applied the IC method to a number of areas of state-selected transition metal chemistry (*22–25*). We use the reactions of Co^+ ions with propane as an example of the method (*22, 23*). The Co^+ ion has a ^3F, $3d^8$ ground state and two

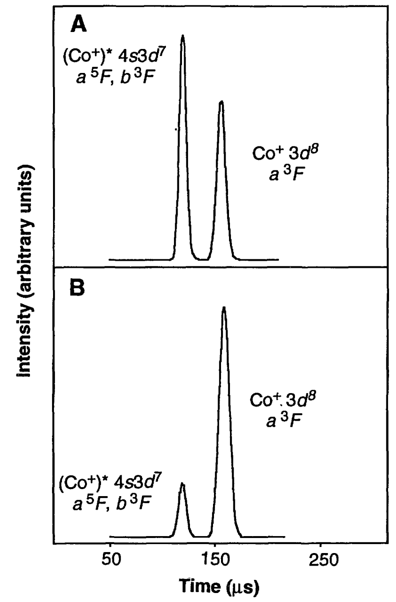

Fig. 2. The ATDs of Co^+ ions that have passed through the IC cell. The ions are formed (**A**) from 75-eV electron impact on $Co(CO)_3NO$, yielding 48% ground state and 52% excited state, and (**B**) by 50-eV electron impact on $CoCp(CO)_2$, forming 83% ground state and 17% excited state.

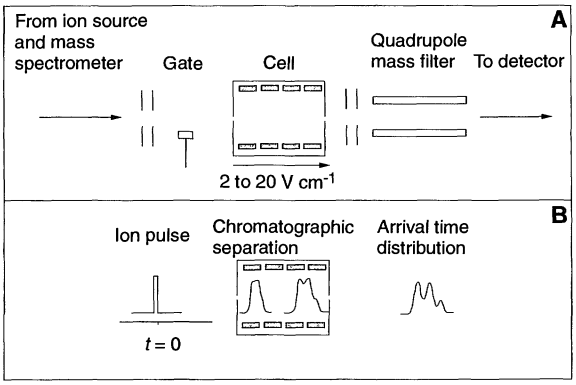

Fig. 1. Ion chromatography experiment. (**A**) Essential elements of the instrument. A beam of mass-selected ions is focused on the 0.5-mm entrance hole of the IC cell, which contains 2 to 5 torr of He. A 1- to 10-μs pulse is injected, typically at low energy (2 or 3 eV, lab frame of reference), and drifts through the cell under the influence of a small electric field. The ions exit the cell, are mass analyzed, and detected. (**B**) Spatial and temporal ion beam profile for a model system. A sharp pulse of ions is formed at $t = 0$, chromatographically separated in the cell, and subsequently detected.

relatively low-lying metastable excited states [^5F, $3d^74s^1$ (+0.43 eV) and ^3F, $3d^74s^1$ (+1.20 eV)]. The short time peak in Fig. 2 corresponds to the ^5F and ^3F excited states, and it is apparent that they are not resolved. However, using a number of techniques, including surface ionization, which formed only the lower energy ^5F state, we were able to show that their reactivity with propane is very similar.

Three reaction channels with propane were observed

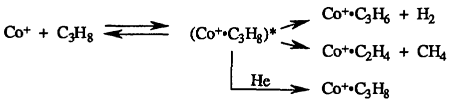

$$Co^+ + C_3H_8 \rightleftharpoons (Co^+{\cdot}C_3H_8)^* \rightarrow Co^+{\cdot}C_3H_6 + H_2;\ Co^+{\cdot}C_2H_4 + CH_4;\ \xrightarrow{He} Co^+{\cdot}C_3H_8$$

By varying the electronic state composition of the reactant Co^+ ions, we could determine state-resolved absolute rate constants for all three product channels (Fig. 3). Adduct formation dominates the ^3F, $3d^8$ ground state reactivity but becomes a minor channel for the ^5F and ^3F, $3d^74s^1$ excited states. This result is consistent with the expectation that the 4s electron will rather strongly destabilize the $Co^+{\cdot}C_3H_8$ electrostatic complex. The larger rates of H_2 and CH_4 elimination for the $3d^74s^1$ excited states relative to the $3d^8$ ground state was unexpected because the 4s electron was thought to increase the energy of the C-H insertion transition state and decrease the elimination rate constants. The observation of enhanced H_2 and CH_4 elimination indicates that the C-H insertion transition states on the excited state surfaces are strongly mixed with the ground state (*26*). This mixing results in substantial stabilization of these transition states relative to the Co^+ (^5F and ^3F, $3d^74s^1$)-C_3H_8 asymptotic energy, leading to the relatively large H_2 and CH_4 elimination rate constants.

Excited state deactivation. In addition to determining state-specific rate constants with the IC technique, we can also obtain information with regard to collisional deactivation of electronically excited states to the ground state. In recent studies of first-row transition metal ions (groups IV to XII), collisional deactivation was observed only for Fe^+, Mn^+, and Ti^+ in He (*18*). In each of these cases, an excited state of $3d^n$ configuration was observed to deactivate to a $4s3d^{n-1}$ ground state. In no case did excited $4s3d^{n-1}$ states collisionally deactivate at thermal energy.

Loh *et al.* (*27*) first proposed that the deactivation occurs by means of a crossing of the potential curves in the M^+-He collision when the M^+ ground state ion has a $4s3d^{n-1}$ configuration and the excited state has a $3d^n$ configuration. The $4s3d^{n-1}$ potential energy curve becomes more repulsive at a larger internuclear distance than the $3d^n$ excited configuration because of the repulsion between the 4s electron and the filled $1s^2$ shell of He. Thus, the potential energy curves cross at long range for the two states, providing a means for deactivation in the collision. Such a crossing does not occur for the $3d^n$ ground states and $4s3d^{n-1}$ excited states.

Table 1. Experimental (*29*) and theoretical (*30*) values of bond dissociation energies D_e and equilibrium bond lengths r_m for $M^{+*}{\cdot}He$ and $M^{+*}{\cdot}Ne$.

System	D_e (kcal mol^{-1})		r_m (Å)	
	Experiment	Theory	Experiment	Theory
Co^{+*} ($3d^74s^1$)·He	0.35 ± 0.06	0.37	2.92 ± 0.2	3.21
Co^{+*} ($3d^74s^1$)·Ne	1.21 ± 0.21	0.74	2.56 ± 0.2	3.06
Ni^{+*} ($3d^84s^1$)·He	0.36 ± 0.06	0.34	2.90 ± 0.2	3.19
Ni^{+*} ($3d^84s^1$)·Ne	1.01 ± 0.20	0.81	2.74 ± 0.2	2.95

Collisional deactivation is observed in the ATD for Fe^+. Unlike the ATD for Co^+, for which two baseline resolved peaks corresponding to ground and excited state Co^+ are observed, the Fe^+ ATD consists of a single peak with a slight tail. The main peak is composed of the ^6D $4s3d^6$ ground state and the ^4D $4s3d^6$ second excited state, and the tail contains the ^4F $3d^7$ first excited state. The ^4F state would have been baseline resolved from the ^6D and ^4D states in the absence of collisional deactivation (Fig. 2). However, collisional deactivation of the ^4F to the ^6D state does occur, giving rise to Fe^+ arrival times intermediate between those of the ^4F and ^6D states. The fraction of the $4s3d^6$ and $3d^7$ electronic state configurations as well as the rate of deactivation of the ^4F state to the ^6D state are accurately and uniquely determined (*23*) by modeling the experimental ATDs with the known transport properties of the ground and excited states of Fe^+.

Ligand binding energies. A further application of the IC method is measurement of equilibrium constants. Consider, for example, reactions of the type

$$M^+ + R \rightleftharpoons M^+{\bullet}R \qquad (5)$$

where M^+ is a transition metal ion and R is a neutral atom or molecule. If there is an unreactive excited state of M^+ (or one in which the equilibrium is strongly shifted toward the reactants) then it is not possible to measure accurate equilibrium constants and obtain ligand binding energies. The IC method can determine immediately whether this is the case and allows acceptable remedies to be applied. For example, the $Co^+{\cdot}H_2$ adduct is strongly bound (18 kcal mol^{-1}) (*28*), and hence the equilibrium in Eq. 5 is strongly to the right. In this case, the Co^+ b^3F and a^5F excited states of $3d^74s^1$ configuration essentially do not cluster with H_2, and collisions with H_2 do not relax these states to the a^3F ($3d^8$) ground state. Even a 3% $3d^74s^1$ impurity required a precise correction (with use of IC) before valid equilibrium constants could be obtained (*28*).

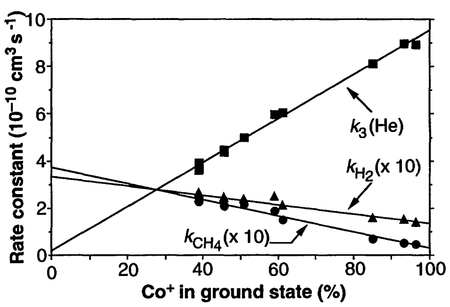

Fig. 3. Absolute rate constants for $CoC_3H_8^+$ adduct formation [k_3(He)] and for H_2 (k_{H_2}) and CH_4 (k_{CH_4}) elimination channels as a function of the percentage of Co^+ in the ground state. The linear least square fit of the experimental data was used to extrapolate to reaction rate constants corresponding to 100% ground state and 100% excited state Co^+.

Sometimes the fact that excited states are not easily relaxed to the ground state by collision can be an advantage. This is the case for all transition metal ions with $3d^n$ ground states and $3d^{n-1}4s^1$ excited states (V^+, Cr^+, Co^+, and Ni^+ are examples) for which collisions with He or Ne are completely ineffective in deactivating the excited state

$$M^{+*}\ (3d^{n-1}4s^1) + He, Ne \not\rightarrow M^+\ (3d^n) + He, Ne \qquad (6)$$

In these instances, the mobility of M^{+*} ($3d^{n-1}4s^1$) can be measured as a function of temperature. Modeling the change in mobility with temperature allows accurate determination of the potential energy curves for these metal ion–rare gas systems (*29*). From these curves, binding energies and equilibrium internuclear distances can be obtained. The agreement between data (*29*) and predictions from high-level ab initio calculations (*30*) (Table 1) is very good, and when it is considered that the level of theory used is expected to give binding energies about 15% below experiment, the agreement is quantitative. In all cases, the species are predicted to be zero point bound, a fact verified by equilibrium measurements (*18*) of the Ni^{+*} ($3d^84s^1$) binding energies to He and Ne, which are in good agreement with the data in Table 1.

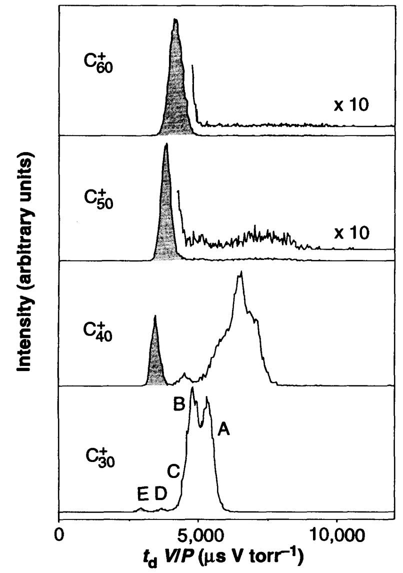

Fig. 4. The ATDs for C_{30}^+, C_{40}^+, C_{50}^+, and C_{60}^+. Five different isomeric families are identified as peaks A, B, C, D, and E. The horizontal axis is proportional to time but is multiplied by the ratio of the drift voltage and cell pressure to compensate for somewhat different experimental conditions in the four spectra. Each peak within a family moves to longer times as mass increases as a result of the mass dependence of the mobility. Principal families: A, monocyclic planar rings; B, bicyclic planar rings; C, tricyclic planar rings; and E, fullerenes (shaded).

Carbon Clusters

One of the most important and interesting problems in cluster research concerns the structure of the cluster and how structure changes with cluster size. This is an extremely difficult problem because most neutral clusters are generated in very broad size distributions, and consequently, even if sufficient quantities are generated, traditional spectroscopic probes can seldom give unambiguous results. Ionic clusters, on the other hand, have the tremendous advantage that they can be easily mass (size) selected and have their properties unambiguously interrogated. Further, for all but the smallest systems, ionic and neutral clusters are expected to have the same structures. Unfortunately, intensities are usually very low for ions and only a few small systems have been investigated by traditional spectroscopic methods. More indirect methods have been applied, however, including reactivity studies, photoelectron spectroscopy of negative ions, measurements of ionization potentials, and observations of so-called "magic numbers" in cluster mass spectra. Each of these methods has provided important information suggestive of ion structure (*31, 32*). The problem with each of them, however, is there is no way to unambiguously connect these data to specific cluster structures.

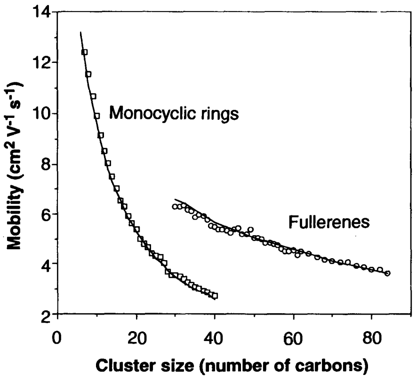

Fig. 5. A plot of the mobility versus cluster size for the monocyclic ring and fullerene families of isomers (peaks A and E in Fig. 4). The excellent agreement between experiment (points) and theory (lines, from model in text) confirms the structural assignments.

When properly analyzed, IC data give unambiguous structural information that allows differentiation of major structural types. We concentrate on carbon clusters because we have the most experience with them and because carbon's incredible bonding flexibility leads to an amazing assortment of interesting structures. Structural variation with size has also been observed for silicon in some elegant experiments by Jarrold and co-workers (*33*).

Experimental. Carbon cluster ions are formed by laser desorption, entrained in a pulse of high-pressure He gas, expanded through a nozzle, accelerated, mass selected, and decelerated. A 2- to 10-μs pulse is then injected at low energy into the IC cell. The ions exiting the cell are quadrupole mass analyzed and detected. In our source, we can make clusters at every C_n unit from $n = 2$ to $n > 100$. Because of the short distance (3 mm) from the laser ablation to the nozzle, the clusters do not have a long time to react; hence, both kinetics and thermodynamics dictate the isomer distribution for a given cluster size, and kinetics dictates the size distribution itself.

It is apparent from the C_{30}^+ and C_{40}^+ data (Fig. 4) that the ATDs are quite complex, and hence a number of structural isomers are present. Peaks A, B, C, D, and E in the C_{30}^+ ATD are also present for C_{40}^+ but shifted to longer times because of the increase in mass. A dramatic change occurs between C_{40}^+ and C_{50}^+ as the long time peaks essentially disappear and only the peak at shortest time (E) remains. This transformation is even more evident in the C_{60}^+ ATD.

Structural assignments. From data such as those in Fig. 4, mobilities can be readily obtained for each of the features (Fig. 5). The mobility decreases in a regular way as size increases for both the A and E sets of peaks, and the rate of change is much greater for A than for E. From these data alone we can say unambiguously that A and E constitute two distinct structural families and that A has lower dimensionality than E.

To get additional, more detailed structural information on these clusters, we developed a structurally specific theoretical model (*34*) that generates mobilities that can be compared with experiment. In essence, we calculate a cluster structure using ab initio or semiempirical methods and ensure that the structure is a minimum on the potential energy surface. We then give each carbon center a fixed van der Waals radius and use Monte Carlo methods to determine the angle-averaged collision cross section with He. The mobility is calculated from this cross section and compared with experiment (Fig. 5). We find that peak A corresponds to a family of monocyclic rings and E to fullerenes. Theory and experiment agree within the combined experimental and theoretical uncertainties (±2%). This procedure, in which there are no variable parameters (*35*), gives us confidence to use IC to get unambiguous structural information on clusters.

Given these results, we can explain the structures of families B, C, and D (Fig. 3). In each case, the mobilities vary in a regular way with cluster size. Peaks B and C have the identical dimensionality as A and hence are planar ring systems (*34*). Modeling indicates B is a family of planar "bicyclic" rings and C, planar "tricyclic" rings (Fig. 6). It is interesting that in each case a new family appears to start when a ring size of 10 is attached (that is, A starts near C_{10}, B near C_{20}, and C near C_{30}).

The family labeled D is intriguing. It never accounts for more than ~5% of the intensity, starts at the improbable size of C_{29}, and ends near C_{55}. It has a dimensionality close to that of the fullerene family and hence is composed of three-dimensional objects. Mobility modeling suggests it may be a three-dimensional ring family with planar rings of different sizes (≥10) attached to a common pair of carbon atoms with the ring planes at 120° to each other. Other possible structures are being investigated, however, and we have no definitive assignment at this time.

Initially, we thought the D family might be an "open" fullerene with a cuplike structure containing hexagons and appropriate numbers of pentagons (Fig. 6). This is an appealing structural family as it could be used to rationalize fullerene formation (*36*), especially C_{60} (*37*). Although quantum chemical calculations (*34, 38, 39*) indicate such cup structures are stable, mobility modeling studies (*34, 38*) indicate they do not correspond to any of the peaks in any of our ATDs at any carbon cluster size (predicted mobilities typically differ from experiment by

7 to 10%, well outside of our error limits). This means that fullerene formation almost certainly does not require nor utilize species of this type and that some other growth mechanism must be responsible.

The mysterious appearance of the fullerenes. In our view, the plasma initially generated by the laser contains a high density of carbon atoms and small carbon fragments. Our data indicate growth of C_n occurs according to

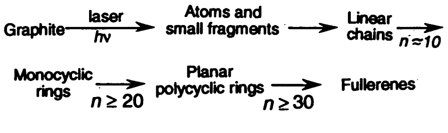

It seems reasonable that carbon atoms should recombine first to form linear chains. At about C_{10}, ring strain apparently becomes less than the energy released by coupling the terminal dangling bonds of the chains, and monocyclic rings become prominent. Small, linear carbon fragments attacking the rings appear to simply produce larger monocyclic rings. At about C_{20}, C_{30}, and C_{40}, new families of planar polycyclic rings appear (*34*). These probably result from the "clipping" together of planar ring systems and account for the rapid growth of carbon clusters in this size range.

The real mystery, then, is the sudden appearance of the first fullerene at C_{30}^+. We have shown that graphitic fragments composed of five- and six-member rings, which could act as fullerene precursors, do not exist at any size range. Thinking that perhaps the ions in the source did not have a sufficiently long time at a sufficiently high temperature to anneal, we annealed clusters in the C_{30}^+ to C_{40}^+ size range (*40, 41*), where fullerenes first appear. In these experiments, C_{35}^+ was injected at high energy into the IC cell. This injection created a large transient heating pulse in the C_{35}^+ and allowed it to rearrange or dissociate, or undergo both processes.

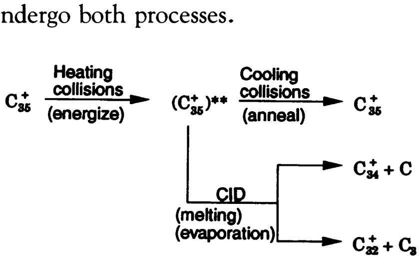

For an injection energy of 150 eV, ~40% of the C_{35}^+ ions experienced collision-induced dissociation (CID), with C_{34}^+ and C_{32}^+ comprising ~80% of the products.

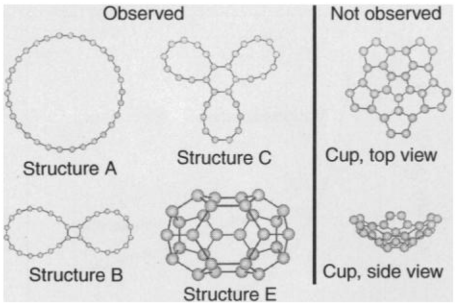

Fig. 6. Structures of a number of isomers of C_{30}. These structures were calculated by semiempirical quantum chemical methods (PM3) and all correspond to minima on the potential surface. Labels A, B, C, and E correspond to the peaks in Fig. 4. The cup structure on the right, proposed for peak D, corresponds to a C_{60} fullerene cut in half and is a minimum on the potential surface. However, these cup structures were not observed in our experiments.

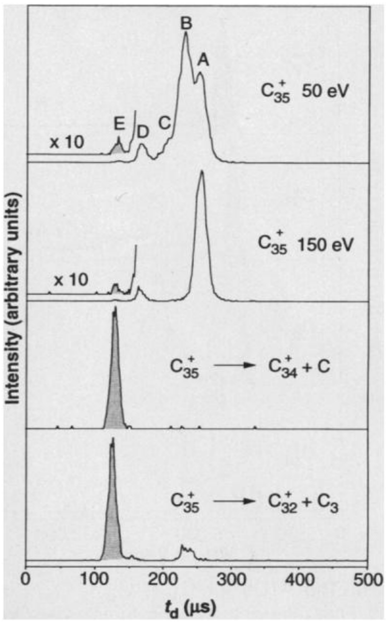

Fig. 7. The ATDs from isomer annealing studies for C_{35}^+. When C_{35}^+ is injected at 50 eV, an energy too low for either isomerization or dissociation to occur, the ATD reveals peaks A, B, and C, corresponding to monocyclic, bicyclic, and tricyclic rings, and E, corresponding to fullerenes (shaded). When C_{35}^+ is injected at 150 eV, the ATD of surviving C_{35}^+ ions shows that bicyclic and tricyclic rings (peaks B and C) are completely gone and monocyclic rings (peak A) dominate. The ATD of the C_{34}^+ product indicates 100% fullerene formation, whereas that for the C_{32}^+ product indicates 85% fullerene and 12% monocyclic ring formation.

The ATD of C_{35}^+ injected at a low energy (50 eV) is dominated by mono- and bicyclic ring structures with only small contributions from three-dimensional isomers (Fig. 7). In the ATD of the C_{35}^+ ions that survived higher energy injection (150 eV), all bi- and tricyclic rings (peaks B and C) are gone, either by dissociation or conversion to monocyclic rings. For the C_{34}^+ formed by means of CID, 100% of the C_{34}^+ ions have the fullerene structure. A similar result appears for the C_{32}^+ product ions formed by loss of C_3. In this case, however, 85% of the ions have the fullerene structure and 12% are monocyclic rings. This latter result shows that monocyclic rings effectively compete with fullerenes at C_{32}^+ and must have comparable energies.

As we increase the size of the injected ion, the fraction that dissociates increases and the percentage of fullerene formed becomes essentially 100% by C_{39}^+. Although the details are discussed elsewhere (*34, 40*), the result is that fullerenes are formed by heating and by the rearrangement of planar ring systems. It appears from our experiments that the crossover in stability from monocyclic rings to fullerenes occurs near C_{30}, in good agreement with theory (*42*). As planar ring systems grow, their barrier to rearrangement into fullerenes decreases until very facile isomerization can occur above C_{60}. The nascent fullerenes formed in this size range are very highly internally excited and cool themselves by evaporation of small carbon fragments. In this evaporation process, C_{60} is favored because it is significantly more stable than its neighbors. The propensity for formation of the most stable products is born out in the data (Fig. 7): excited $(C_{35}^+)^*$ loses C_1 and C_3 to form C_{34}^+ and C_{32}^+ fullerenes, but no products of any kind are observed for C_{33}^+.

Summary and Prognosis

The application of IC to both metal ions and clusters has a bright future given the many transition metals available and the great variety of atomic and molecular clusters that can be investigated. This is especially true for clusters, where ions and neutrals almost certainly have the same structures, especially for larger sizes. One qualitatively new area that might in fact prove to be the most interesting is the structure of macromolecules.

Biologically important molecules are of particular interest. They can now be routinely transported intact from solution to the gas phase with electrospray or a variety of other techniques. Some clever methods have been introduced to determine the gross structure of some of these species, but no unambiguous results have yet been forthcoming. We have done preliminary molecular mechanics simulations of structures of simple polypeptides, and the results indicate IC methods should easily be able to distinguish between isomeric forms that have significant structural differences. Many questions immediately come to mind, such as the importance of solvent in the determination of protein structure and the possibility of structural change with the number of charges localized on the molecule (electrospray typically generates a broad distribution of charges on the monomer). These are important questions, and IC is a promising tool with which we can address these issues.

REFERENCES AND NOTES

1. J. C. Maxwell, *Philos. Mag.* **20**, 21 (1860).
2. P. Langevin, *Ann. Chim. Phys.* **5**, 245 (1905).
3. G. H. Wannier, *Bell Syst. Tech. J.* **32**, 170 (1953); *Phys. Rev.* **83**, 281 (1951); **87**, 795 (1952).
4. H. S. W. Massey, *Electronic and Ionic Impact Phenomena* (Clarendon, Oxford, 1969), vol. II.
5. L. B. Loeb, *Basic Processes of Gaseous Electronics* (Univ. of California Press, Berkeley, CA, 1960).
6. E. W. McDaniel and E. A. Mason, *The Mobility and Diffusion of Ions in Gases* (Wiley, New York, 1973); see also E. A. Mason and E. W. McDaniel, *Transport Properties of Ions in Gases* (Wiley, New York, 1988).
7. H. H. Hill Jr., W. F. Siems, R. H. St. Louis, D. G. McMinn, *Anal. Chem.* **62**, 1201 (1990).
8. R. H. St. Louis and H. H. Hill, *Crit. Rev. Anal. Chem.* **21**, 321 (1990).
9. G. A. Eiceman, *ibid.* **22**, 17 (1991).
10. Z. Karpas, *Forensic Sci. Rev.* **1**, 103 (1990).
11. P. R. Kemper and M. T. Bowers, *J. Am. Soc. Mass Spectrom.* **1**, 197 (1990).
12. N. Aristov and P. B. Armentrout, *J. Am. Chem. Soc.* **109**, 1806 (1986).
13. P. R. Kemper and M. T. Bowers, in preparation.
14. T. G. Dietz, M. A. Duncan, D. E. Powers, R. E. Smalley, *J. Chem. Phys.* **74**, 6511 (1981); V. E. Bondybey and J. H. English, *ibid.* **76**, 2165 (1982).
15. P. P. Radi, G. von Helden, M.-T. Hsu, P. R. Kemper, M. T. Bowers, *Int. J. Mass Spectrom. Ion Processes* **109**, 49 (1991).
16. The quantity σ is really the collision cross section only for "hard sphere" collisions of large ions with He. For smaller species, such as transition metal ions, σ is really the collision integral, which requires consideration of the details of the interaction potential.
17. Equation 2 holds for heavy ions colliding with light neutrals for relatively low values of E. These conditions are fulfilled for all systems reported in this article.
18. P. R. Kemper and M. T. Bowers, *J. Phys. Chem.* **95**, 5134 (1991).
19. ______, *J. Am. Chem. Soc.* **112**, 3231 (1990).
20. Early papers that document the involvement of excited electronic states: W. D. Reents, Jr., F. Stroble, R. B. Freas, J. Wronka, D. P. Ridge, *J. Phys. Chem.* **89**, 5666 (1985); J. L. Elkind and P. B. Armentrout, *ibid.*, p. 5626.
21. For a recent review, see P. B. Armentrout, *Annu. Rev. Phys. Chem.* **41**, 313 (1990).
22. P. A. M. van Koppen, P. R. Kemper, M. T. Bowers, *J. Am. Chem. Soc.* **114**, 1083 (1992).
23. ______, *ibid.*, p. 10941.
24. P. R. Kemper, M.-T. Hsu, M. T. Bowers, *J. Phys. Chem.* **95**, 10600 (1991).
25. P. A. M. van Koppen, P. R. Kemper, M. T. Bowers, *J. Am. Chem. Soc.*, in press.
26. P. A. M. van Koppen, *et al.*, *ibid.* **112**, 5663 (1990); *ibid.* **115**, 2359 (1991).
27. S. K. Loh, E. R. Fisher, L. Lian, R. H. Schultz, P. B. Armentrout, *J. Phys. Chem.* **93**, 3159 (1989).
28. P. R. Kemper, J. Bushnell, G. von Helden, M. T. Bowers, *ibid.* **97**, 52 (1993).
29. G. von Helden, P. R. Kemper, M.-T. Hsu, M. T. Bowers, *J. Chem. Phys.* **96**, 6591 (1992).
30. H. Partridge, C. W. Bauschlicher, Jr., S. R. Langhoff, *J. Phys. Chem.* **96**, 5350 (1992).
31. W. Weltner and R. van Zee, *Chem. Rev.* **89**, 1713 (1989), and references therein.
32. D. C. Parent and S. L. Anderson, *ibid.* **92**, 1541 (1992), and references therein.
33. For a recent summary, see M. F. Jarrold, *Science* **252**, 1085 (1991).
34. For detail on the structural model and in-depth discussion on mobility versus cluster size, see G. von Helden, M.-T. Hsu, N. G. Gotts, M. T. Bowers, *J. Phys. Chem.*, in press; see also G. von Helden, M.-T. Hsu, P. R. Kemper, M. T. Bowers, *J. Chem. Phys.* **95**, 3835 (1991).
35. Actually, the sum of the van der Waals radii of C and He needed to be specified for the calculations. On the basis of published values, we chose 1.15 Å for He and 1.55 Å for C for a sum of 2.7 Å, which then was not varied.
36. H. W. Kroto, J. R. Heath, S. C. O'Brien, R. F. Curl, R. E. Smalley, *Nature* **318**, 162 (1985), Q. L. Zhang *et al. J. Phys. Chem.* **90**, 525 (1986).
37. R. E. Smalley, *Acc. Chem. Res.* **25**, 97 (1992).
38. G. von Helden, M.-T. Hsu, N. G. Gotts, P. R. Kemper, M. T. Bowers, *Chem. Phys. Lett.*, in press.
39. C. J. Brabec *et al.*, *Phys. Rev. B* **46**, 7326 (1992).
40. G. von Helden, N. G. Gotts, M. T. Bowers, *Nature* **363**, 60 (1993); *J. Am. Chem. Soc.*, in press.
41. The first annealing studies in which IC was used were reported by M. F. Jarrold and H. C. Honea [*J. Am. Chem. Soc.* **114**, 459 (1992)].
42. M. Feyereisen, M. Gutowski, J. Simons, J. Almlöf, *J. Chem. Phys.* **96**, 2926 (1992); see also X. Jing and J. R. Chelikowski, *Phys. Rev. B* **46**, 15503 (1992).

43. Supported by National Science Foundation grant CHE92-19752 and Air Force Office of Scientific Research grant AFOSR92-J-0021.

True Atomic Resolution by Atomic Force Microscopy Through Repulsive and Attractive Forces

F. Ohnesorge and G. Binnig

The $(10\bar{1}4)$ cleavage plane of calcite has been investigated by atomic force microscopy in water at room temperature. True lateral atomic-scale resolution was achieved; the atomic-scale periodicities as well as the expected relative positions of the atoms within each unit cell were obtained. Along monoatomic step lines, atomic-scale kinks, representing point-like defects, were resolved. Attractive forces on the order of 10^{-11} newton acting between single atomic sites on the sample and the front atoms of the tip were directly measured and provided the highest, most reliable resolution on a flat, well-ordered surface.

Atomic force microscopy (AFM) (*1, 2*) is capable of resolving surface structures of both conductors and insulators on the atomic scale in air, in ultrahigh vacuum (UHV), and in liquids [for an overview see (*3–5*)]. The development of AFM in liquids by the group of Hansma (*6*) has largely extended the range of applications for this technique especially in the fields of biology (*7–9*) and electrochemistry (*10*). Imaging surfaces by AFM has proven to be a powerful tool in a number of fields [for an overview, see: (*3–5, 11, 12*)] because many materials under certain conditions are not accessible by any other technique in the size range from <1 to 50 nm. Many atomic-scale images of crystalline solids taken by AFM have been published. However, most of the reported data show either perfectly ordered periodic atomic structures or defects on a larger lateral scale, but no well-defined, laterally resolved atomic-scale defects like those seen in images routinely obtained with scanning tunneling microscopy (STM). Although STM and AFM are very much alike in many respects, there are significant differences between the two methods, and the question has been raised whether the AFM is really a microscope like the STM with true atomic resolution (*3*).

In this article we describe investigations on calcite ($CaCO_3$) in water at room temperature. Calcite has already been studied by AFM in liquids. The main emphasis has been on crystal growth and dissolution processes on the atomic scale (*13*), but some studies have focused on atomic-surface structure analysis (*14*). In the results presented here, well-defined defects were observed with true atomic-scale lateral resolution. This resolution could only be achieved when the estimated net repulsive loading force exerted on the sample by the front atoms of the tip was 10^{-10} N or lower. Upon increasing the force, we observed that monoatomic steplines were slowly wiped away and a perfectly ordered surface was left (*15*). This observation explains why mostly defect-free atomic resolution has been observed with AFM. In most of the reported results, repulsive forces greater than 10^{-10} N have been applied by the front atoms of the tip.

Experimental Results

We used a home-built AFM with optical lever detection as described briefly in (*16*) together with commercially available (*17*) force sensors with integrated tips. Calcite cleaves easily to form a macroscopic $(10\bar{1}4)$ cleavage rhombohedron. The structure of the $(10\bar{1}4)$ cleavage plane, which does not cross any of the strong covalent C–O bonds, is shown in Fig. 1 as derived from the three-dimensional crystal data (*18*).

The authors are in the IBM Research Division, Physikgruppe München, Schellingstrasse 4, 8000 München 40, Federal Republic of Germany.